Experimental and Numerical Determination of Micropropulsion Device Efficiencies at Low Reynolds Numbers

Andrew D. Ketsdever[†]

Air Force Research Laboratory, Propulsion Directorate, Edwards Air Force Base, California 93524

Michael T. Clabough[*], Sergey F. Gimelshein[‡], Alina Alexeenko[º]

Department of Aerospace and Mechanical Engineering, University of Southern California, Los Angeles, California 90089-1191

Abstract:

The need for low thrust propulsion systems for maneuvers on micro- and nano-spacecraft is growing. Low thrust characteristics generally lead to low Reynolds number flows from propulsive devices that utilize nozzle expansions. Low Reynolds number flows of helium and nitrogen through a small conical nozzle and a thin-walled orifice have been investigated both numerically, using the Direct Simulation Monte Carlo technique, and experimentally, using a nano-Newton thrust stand. For throat Reynolds number less than 100, the nozzle to orifice thrust ratio is less than unity; however, the corresponding ratio of specific impulse remains greater than one for the Reynolds number range from 0.02 to 200. Once the Direct Simulation Monte Carlo

---

[†] Group Leader, Aerophysics Branch, 10 E. Saturn Blvd., Senior Member AIAA. e-mail: andrew.ketsdever@usafa.af.mil
[*] Graduate Research Assistant.
[‡] Research Professor, 854 W. 36th Place, Member AIAA. e-mail: gimelshe@usc.edu
[º] WISE Postdoctoral Fellow, Member AIAA. e-mail: alexeenk@usc.edu

Report Documentation Page

Form Approved
OMB No. 0704-0188

1. REPORT DATE	2. REPORT TYPE	3. DATES COVERED
OCT 2004		-

4. TITLE AND SUBTITLE	5a. CONTRACT NUMBER
Experimental and Numerical Determination of Micropropulsion Device Efficiencies at Low Reynolds Numbers	5b. GRANT NUMBER
	5c. PROGRAM ELEMENT NUMBER
6. AUTHOR(S)	5d. PROJECT NUMBER
A Ketsdever; M Clabough; S Gimelshein; A Alexeenko	**2308**
	5e. TASK NUMBER **M19B**
	5f. WORK UNIT NUMBER
7. PERFORMING ORGANIZATION NAME(S) AND ADDRESS(ES)	8. PERFORMING ORGANIZATION REPORT NUMBER
Air Force Research Laboratory (AFMC),AFRL/PRSA,10 E. Saturn Blvd.,Edwards AFB,CA,93524-7680	
9. SPONSORING/MONITORING AGENCY NAME(S) AND ADDRESS(ES)	10. SPONSOR/MONITOR'S ACRONYM(S)
	11. SPONSOR/MONITOR'S REPORT NUMBER(S)

12. DISTRIBUTION/AVAILABILITY STATEMENT

Approved for public release; distribution unlimited

13. SUPPLEMENTARY NOTES

14. ABSTRACT

The need for low thrust propulsion systems for maneuvers on micro- and nano-spacecraft is growing. Low thrust characteristics generally lead to low Reynolds number flows from propulsive devices that utilize nozzle expansions. Low Reynolds number flows of helium and nitrogen through a small conical nozzle and a thin-walled orifice have been investigated both numerically, using the Direct Simulation Monte Carlo technique, and experimentally, using a nano-Newton thrust stand. For throat Reynolds number less than 100, the nozzle to orifice thrust ratio is less than unity; however, the corresponding ratio of specific impulse remains greater than one for the Reynolds number range from 0.02 to 200. Once the Direct Simulation Monte Carlo model results were verified using experimental thrust and mass flow data, the model was used to investigate the effects of geometrical variations on the conical nozzle's performance. At low Reynolds numbers, improvements to the specific impulse on the order of 4 to 8% were achieved through a combination of decreasing the nozzle length and increasing the nozzle expansion angle relative to the nominal experimental geometry.

15. SUBJECT TERMS

16. SECURITY CLASSIFICATION OF:			17. LIMITATION OF ABSTRACT	18. NUMBER OF PAGES	19a. NAME OF RESPONSIBLE PERSON
a. REPORT	b. ABSTRACT	c. THIS PAGE			
unclassified	**unclassified**	**unclassified**		**46**	

model results were verified using experimental thrust and mass flow data, the model was used to investigate the effects of geometrical variations on the conical nozzle's performance. At low Reynolds numbers, improvements to the specific impulse on the order of 4 to 8% were achieved through a combination of decreasing the nozzle length and increasing the nozzle expansion angle relative to the nominal experimental geometry.

Nomenclature

α	=	fraction of molecules reflected diffusely from a surface
A	=	area, m^2
d	=	diameter, m
γ	=	ratio of specific heats
Isp	=	specific impulse, sec
k	=	Boltzmann's constant = $1.3806503 \times 10^{-23}$ J/K
L	=	nominal length of the diverging section of the nozzle, m
l_w	=	nominal length of the diverging section wall of the nozzle, m
m	=	molecular mass, kg
μ	=	viscosity, kg/m^2s
M	=	Mach number
n	=	unit vector normal to a surface
ρ	=	density, kg/m^3
p	=	pressure, Pa
Re	=	Reynolds number
t	=	orifice thickness, m

T	=	temperature, K
$\Im$	=	thrust, N
$\boldsymbol{\tau}$	=	unit vector tangential to a surface
θ	=	divergent half angle of the nozzle
u	=	axial velocity, m/s
v	=	radial velocity component, m/s
$\mathbf{v}$	=	velocity vector
ω	=	viscosity exponent

Subscripts

0	=	plenum or stagnation
c	=	curvature
cont	=	continuum
e	=	exit condition
fm	=	free molecular
o	=	orifice
n	=	nozzle
η	=	value normal to a surface
ref	=	reference value
t	=	throat condition
τ	=	value tangential to a surface
w	=	wall
x	=	axial component

Superscripts

* = sonic condition

overbar= mean value

prime = after collision value

Introduction

Future micro- and nanosatellites will require low thrust propulsion systems for orbital maneuvers to counter the effects of trajectory perturbations and for fine attitude control. Micropropulsion systems for these vehicles are expected to have thrust in the range from 1 μN to 1 mN. For propulsion systems that utilize nozzle expansions, the low thrust levels will require either low pressure operation or a decrease in the throat dimensions, both potentially leading to low Reynolds number flows. The further development of efficient micro-chemical and electrothermal thrusters is associated with high stagnation chamber temperatures, which will also continue the trend toward decreasing the Reynolds number. Therefore, the numerical and experimental investigation of low Reynolds number flows has become increasingly important for designing efficient, low thrust nozzles.

It is well known that the Reynolds number is a measure of the nozzle efficiency in terms of the viscous losses inherent in the subsonic layer near nozzle surfaces. At sufficiently low Reynolds numbers, the viscous losses within a micronozzle become large enough for the specific impulse along the nozzle centerline to decrease from the nozzle throat to the exit plane[1], perhaps making the divergent nozzle contour useless. In the transitional flow regime, therefore, a thin-walled sonic orifice may outperform, or at least perform as well as, a typical micronozzle.

Although there is extensive literature related to rarefied orifice flows, there have been relatively few investigations of orifice performance in terms of propulsive parameters such as thrust and specific impulse.[2,3] Investigations of low Reynolds number flows through nozzles of various geometric shapes are numerous, with several notable computational efforts[1,4-8] and experimental studies[9-13] having been performed. The Navier-Stokes (NS) equations with velocity slip and the direct simulation Monte Carlo (DSMC) method are typically used to model low Reynolds number flows. For very low Reynolds numbers corresponding to transitional flow, reliable results can only be obtained using a kinetic approach. A previous study has verified that the numerical results obtained with a DSMC flow solver reproduced the experimental data of Rothe[10] while the solution of the NS equations with no-slip boundary conditions did not.[1]

Numerical simulations referenced above have shown that a viscous layer occupies a significant fraction of a nozzle's diverging section for throat Reynolds numbers less than about 500. As the Reynolds number further decreases, the viscous interactions dominate the internal nozzle flow field, limiting nozzle efficiency. Because an orifice with a small thickness to diameter ratio will have a reduced viscous interaction layer, it may provide an adequate propulsive efficiency relative to a nozzle expansion at low Reynolds numbers.

The main goal of this work is to study experimentally and numerically the performance of a thin-walled, squared edge orifice and a DeLaval nozzle in the transitional flow regime. The primary objectives are to compare the relative performance of the nozzle and orifice geometries, find the range of Reynolds numbers where the gas expansion through a micronozzle geometry is no longer valid from an efficiency standpoint, and investigate design parameters such as expansion angle and length which can improve micronozzle performance at low Reynolds

numbers. The study also extends the low end of the Reynolds number range, compared to previous studies, by extending operating conditions down to the free molecule flow regime.

Orifice and nozzle thrust for an inviscid flow

To compare micronozzle and orifice performance, as prescribed above, it is advantageous to use the relative thrust or Isp ratios at a specified pressure or throat Reynolds number. The Reynolds number at a nozzle throat or a thin-walled orifice exit plane is defined as

$$\mathrm{Re}^* = \frac{\rho^* u^* d_t}{\mu^*} \quad (1)$$

The throat density, ρ^*, and the throat velocity, u^*, are calculated from measured stagnation conditions and the quasi one-dimensional flow relations. The viscosity at the throat or orifice exit plane is

$$\mu^* = \left(\mu_{ref} \frac{T_0 \frac{2}{\gamma+1}}{T_{ref}} \right)^{\omega} \quad (2)$$

Thruster performance is determined by considering the thrust and Isp ratio between a nozzle and a thin-walled orifice case with the same stagnation conditions. There are two limits that need to be considered, free molecular and continuum. The free molecule analytical solution for an infinitely thin orifice case is

$$\Im_{o,fm} = \frac{1}{2} p_0 A_o \quad (3)$$

There is no analytical solution available for the free molecule nozzle case, since it depends inherently on the nozzle geometry and gas-surface interactions.

Assuming there is no background pressure, the isentropic continuum thrust from an infinite expansion ratio nozzle is

$$\Im_{n,cont} = \gamma \left[\left(\frac{2}{\gamma - 1} \right) \left(\frac{2}{\gamma + 1} \right)^{\gamma + 1 / \gamma - 1} \right]^{1/2} p_0 A_t \qquad (4)$$

Between these two limits, the computational thrust is calculated for zero background pressure as

$$\Im = \rho_e \overline{u_e^2} A_e = \rho_e (\bar{u}_e^2 + RT_{x,e}) A_e \qquad (5)$$

This expression is usually reduced to $\Im = (\rho_e \bar{u}_e^2 + p_e) A_e$ for finite Reynolds numbers with supersonic conditions, which cannot be used for the nearly sonic cases considered here. Therefore, Eq. 5 is utilized for thrust calculations in this work. To calculate the thrust from a nozzle or orifice from Eq. 5 using a NS solver, one needs to implement the formulation of the NS equations with separate temperature components.

Experimental Setup

All thrust measurements were performed on the nano-Newton Thrust Stand (nNTS) which has been described in detail by Jamison, et. al.[14] The nNTS was installed in Chamber IV of the Collaborative High Altitude Flow Facilities (CHAFF-IV) which is a 3 m diameter by 6 m long cylindrical, high vacuum chamber. The facility was pumped with a 1 m diameter diffusion pump with a pumping speed of 42,000 L/s for helium and 25,000 L/s for molecular nitrogen.

The ultimate facility pressure was approximately 10^{-6} Torr with all operational pressures below 10^{-4} Torr. A previous study[15] has shown that at these background pressures and corresponding thrust levels there is no evidence of background pressure effects on the thrust measurements in CHAFF-IV.

The thin-walled orifice used in this study is shown schematically in Fig. 1. The 1 mm diameter orifice was attached to a plenum with a cross-sectional area much larger than the orifice area to help ensure uniform flow. The orifice was machined in a 0.015 mm thick tantalum shim giving $t/d = 0.015$. The thin-walled geometry was chosen to minimize the viscous effects in the orifice flow.

The conical De Laval nozzle used in this study is shown schematically in Fig. 2. The conical nozzle was scaled from the geometry used by Rothe.[10] The scaled Rothe geometry has a 30° subsonic section, a relatively sharp 1mm diameter throat with radius of curvature $r_c = \frac{d_t}{4}$, a 20° diverging section, and an expansion ratio of 62.4. This geometry was selected due to the extensive experimental data that exists[10] which was previously used to verify the DSMC model's accuracy.[1] The nozzle was machined from aluminum and attached to a cylindrical aluminum plenum and mounted on the nNTS. Figure 3 shows a scanning electron microscope image of the nozzle side wall where the surface features caused by the machining process are clearly evident. The effect of the rough diverging section walls on the nozzle's performance will be investigated in the following sections.

The stagnation pressures for the orifice and nozzle were measured inside their respective plenums using calibrated pressure transducers. The propellant was introduced to the plenum through an adjustable needle valve located downstream of a mass flow meter. In the experimental configuration, the mass flow meters were operated in the continuum regime

throughout the pressure range investigated. The propellants used were molecular nitrogen and helium. In this study, the stagnation pressures ranged from several milliTorr to approximately 17 Torr for both propellants, and the stagnation temperature was measured to be 295 K. The combination of stagnation pressure and temperature gave maximum Reynolds numbers of 350 for nitrogen and about 150 for helium.

The nNTS was calibrated using the gas dynamic and electrostatic calibration techniques described by Selden and Ketsdever,[16] which have been validated through experimental and numerical analysis. A unique feature of the nNTS is its ability to measure the force levels of the 1.0 mm orifice and nozzle geometries from the free molecule through continuum range. The low thrust measuring capability of the nNTS allowed for the investigation of the transitional flow regime overlooked in previous low Reynolds number nozzle studies.

Numerical method

The flow and geometric conditions of the experimental setup described above were simulated and used for validation of the DSMC models and parameters. All walls were assumed to be at a temperature of 295K (as measured in the experiments), and the gases considered include helium and nitrogen at a stagnation temperature of 295K. A background pressure of zero was assumed in the calculations. The throat Reynolds numbers ranged from 0.02 to 270 to adequately cover the range of the experimental data. After the numerical model was analyzed, it was used to study the impact of nozzle parameters of interest. First, the half angle of the diverging section of the nozzle was varied from the experimental case ($\theta = 20°$) to 25°, 30°, and

40° while keeping the wall length, l_w, constant. Second, the nozzle diverging section length was then shortened from the experimental length to L/2 and L/3.

The SMILE computational tool based on the DSMC method was used in the numerical part of this work. Details on the tool may be found elsewhere.[17] The SMILE capabilities that were used in the present work include two-level rectangular grids adaptive to flow gradients, different grids for collisions and macroparameters, and parallel implementation with a static load balancing technique. The majorant frequency scheme was employed for modeling molecular collisions,[18] and the variable hard sphere model was used for modeling intermolecular interactions. The discrete Larsen-Borgnakke model[19-20] with temperature-dependent rotational relaxation number was utilized for rotation-translation energy transfer. The Maxwell model with different values of accommodation coefficients was used to model gas-surface interaction. The background cell size was a fraction of the mean free path at the throat conditions. Over 2 million simulated particles were used in the nozzle cases, and over 6 million particles were used in the orifice cases.

The difficulty with calculations involving subsonic boundary conditions is attributed to the upstream influence of the downstream flow. To deal with these effects, results must be independent of the domain size. For the orifice, the simulated plenum (subsonic section) was varied in the axial direction from $3\,d_t$ to $9\,d_t$ and in the radial direction from $4\,d_t$ to $8\,d_t$ with an exit plane Reynolds number of 200 to show that the macro-parameters at the exit are independent of the plenum size. The simulated plenum size was then chosen to be $9\,d_t$ x $8\,d_t$ for all cases. The computational domain beyond the orifice exit plane (simulated vacuum facility domain) was varied in the axial direction from $11\,d_t$ to $15\,d_t$ and in the radial direction from $5\,d_t$ to $30\,d_t$ to show the independence of the results relative to the vacuum facility domain size. The simulated

vacuum facility domain was then chosen to be 11 d_t x 8 d_t. An equilibrium distribution with values of stagnation pressure and temperature and zero average velocity was used at the top and left boundaries of the plenum in all orifice calculations.

For the nozzle, the computational domain beyond the exit plane (exhausting into the vacuum facility) was varied in the axial direction from 2 d_t to 20 d_t and in the radial direction from 1 d_t to 11 d_t above the exit. The effect of having a larger downstream region was examined and determined to have negligible effect. This exit region was then chosen to go 2 d_t beyond the exit and 1 d_t above the exit. To study the effect of the subsonic inflow condition, computations were performed for a plenum of 5 d_t x 5 d_t and for inflow boundaries located at M = 0.1 and 0.3. The effect on the nozzle thrust with a throat Reynolds number of 200 was found to be negligible. The computed thrust for $\mathrm{Re}^* = 60$ was found to be up to 3% different for the subsonic boundaries located at M = 0.1 and 0.3 compared to thrust computed with the plenum domain included. The difference was due to the impact of the viscous interaction layer in the converging section. Therefore, the plenum geometry was used throughout the remainder of this study, and the plenum dimensions remained constant for all subsequent simulations.

Results and Discussion

A. Orifice and nozzle flow structure

First, the flow structure for the two geometries under consideration with different gas densities, or Reynolds numbers, is examined numerically. Note that the results in this section are shown for helium flows only, since the general flow structure for nitrogen is qualitatively similar for the same Reynolds number. The predicted Mach number contours for the orifice geometry with $\mathrm{Re}^* = 10$ and 200 are presented in Fig. 4. Only a fraction of the computational domain is

shown here in order to illustrate the details of the flow close to the orifice plane. In the figure, the plenum is located to the left of the orifice plane, and the vacuum facility domain is to the right.

The area of the flow impact upstream of the orifice is comparatively small, and the gas is essentially undisturbed at distances larger than two orifice diameters. The impact of the Reynolds number on the subsonic part of the flow (in the plenum) is visible but not large, with the difference in the Mach number amounting to about 40 percent when the Reynolds number increases from 10 to 200. The flow becomes supersonic at a small distance downstream from the orifice. The downstream distance of the sonic line increases slightly with Reynolds number. A much larger number of collisions in the plume for $\mathrm{Re}^* = 200$ results in a significantly lower translational temperature downstream from the orifice, which explains the higher Mach number values when compared to the $\mathrm{Re}^* = 10$ case.

The impact of the Reynolds number and rarefaction effects is more pronounced for the nozzle flow because of gas-surface interactions resulting in fully viscous flow. The chamber gas mean free path for $\mathrm{Re}^* = 10$ is about $10^{-4}\,m$, which gives a Knudsen number of approximately 0.1 based on the throat diameter. The gas rarefaction for this Knudsen number is high enough for the nozzle surface to influence the gas in the diverging and converging sections. This is clearly seen in Fig. 5 where the Mach number contours are shown for $\mathrm{Re}^* = 10$ and 200. The surface effects in the diverging nozzle section result in subsonic flow in a majority of the section, with a Mach number at the nozzle exit of about 1.3.

For the largest Reynolds number considered, $\mathrm{Re}^* = 200$, the nozzle flow is also dominated by surface interactions. In this case however, an inviscid core starts to form, and the sonic line is located close to the nozzle throat. Still, the viscous interaction layer is very large and

visible even in the converging section. At the nozzle exit, the Mach number drops from about 3.2 at the nozzle exit to less than unity at the lip.

Relatively large mean free paths and strong surface effects cause a significant nonequilibrium between translational modes in both the orifice and the nozzle flows. The extent of flow nonequilibrium is illustrated in Fig. 6, where the ratio of T_x (the temperature calculated using only particle velocities in the axial direction) to the overall translational temperature T is presented for the orifice geometry. It is seen that for $\mathrm{Re}^* = 10$ there is a significant degree of translational mode nonequilibrium inside the plenum. In the core flow downstream from the orifice, the temperature in the axial direction is significantly larger than that in the radial direction due to the flow expansion (the axial component of velocity is largest closer to the axis). The radial component is larger for the flow angles larger than about 45° from the axis.

For a nozzle flow expanding into a vacuum, a strong thermal nonequilibrium in the region of the nozzle lip and in the back flow region is usually expected. For rarefied flows examined in this work, the gas is in thermal nonequilibrium even inside the converging section of the nozzle as shown in Fig. 7. For $\mathrm{Re}^* = 10$, the T_x / T ratio inside the nozzle reaches a maximum of 1.13 near the center of the diverging section and a minimum of 0.78 near the nozzle lip. Thermal nonequilibrium is less significant for $\mathrm{Re}^* = 200$. Nevertheless, the minimum value inside the nozzle of 0.7 is less than for $\mathrm{Re}^* = 10$, substantiating the use of a kinetic approach for numerical modeling of these flows.

A more quantitative illustration of the rarefaction effect of the flow at the orifice plane is given in Fig. 8, where the profiles of the axial velocity are presented for Re^* = 10, 60 and 200. Hereafter $Y = 0$ corresponds to the axisymmetric centerline. For the most rarefied flow, $\mathrm{Re}^* = 10$, the velocity reaches the maximum of 720 m/s on axis, and then decreases toward the

lip; however, the behavior changes qualitatively for larger Reynolds numbers. For $\mathrm{Re}^* = 60$ and $\mathrm{Re}^* = 200$, there is a maximum at about $Y = 0.4$ mm, and the velocity at the axis is 10 to 20 percent lower than the maximum value. The maximum in the axial velocity is due to the low density expansion region above the plenum (large angles from the centerline). The molecules from that region have a very low probability of backscattering to the plenum compared to the molecules that leave the orifice near the centerline. Therefore, the impact of the returned molecules is lower at larger radial distances.

The axial velocity profiles across the nozzle exit are shown in Fig. 9. It is interesting to note that whereas the velocity is much larger on the nozzle axis for $\mathrm{Re}^* = 200$ than for $\mathrm{Re}^* = 10$, the velocity is only weakly dependent on the Reynolds number at the nozzle lip. For all cases under consideration, the axial velocity tends to decrease with radial distance.

B. Comparison of experimental and numerical results

The comparative performance analysis of an orifice and a nozzle has been conducted numerically and experimentally at different conditions in the free molecular and transitional flow regimes. The computational results for helium flow over the entire range of Reynolds numbers considered are given in Table 1. As expected, thrust and specific impulse increase with increasing Reynolds number for both the orifice and nozzle. The rate of this increase, however, is different for these geometries. As a result, the relative performance, represented by the ratio of the nozzle to orifice thrusts and specific impulses, has a minimum.

Consider the mechanisms that govern the relative performance characteristics for different Reynolds numbers. At large Reynolds numbers, where the flow is near-continuum and the surface effects are less pronounced, the thrust ratio should approach some continuum limit

value. The increase in flow rarefaction causes a larger impact of the surface, and the surface effect is more important in the nozzle geometry, where the surface to volume ratio is much larger than for the orifice.

In the opposite limit of the free molecular flow, the nozzle geometry and the gas-surface interaction law primarily influence the thrust ratio. It may generally be much larger than unity for a specular surface, and less than unity for a diffuse surface. In the presence of molecular collisions, when the flow becomes transitional, the thrust ratio is expected to decrease as the viscous interaction layer inside the nozzle becomes important. As a result, a minimum is observed between the free molecular and continuum limits. An interesting fact is that the minimum is located about a Reynolds number of 10 for the thrust ratio, and 60 for the specific impulse ratio.

The orifice and nozzle thrust in the free molecular and early transitional regime has been examined in more detail. The obtained numerical results have been compared with the experimental measurements in Figures 10 and 11, which present a comparison for a helium flow inside the orifice and the nozzle, respectively, in the range of Reynolds numbers from 0.02 (free molecular regime) to 23. Note that the orifice results, both experimental and computed, begin to deviate from free molecule theory at Reynolds numbers greater than one and remain lower than the corresponding sonic nozzle continuum value at $Re > 20$.

The experimental and numerical results show that the nozzle thrust does not yet approach its continuum value by a Reynolds number of 20, with the difference of about a factor of two as shown in Fig. 11. The difference between the measurements and the calculations is somewhat larger for the nozzle than for the orifice, with the experimental slope being steeper. This

difference is attributed primarily to the gas-surface interaction model used in the computations as discussed in more detail below.

Comparison of the numerical and experimental results in a wider range of Reynolds numbers is presented in Fig. 12, where the nozzle-to-orifice thrust ratio is given for a helium flow. Comparison of the experimental data with the modeling results for fully diffuse walls shows that the calculations are in good agreement with the data at larger Reynolds numbers and overpredict it at lower pressures. The numerical error due to statistical scatter, convergence issues, and boundary conditions is estimated to be on the order of one percent in a single thrust value and two percent in the thrust ratio. The reason for the difference in the slope, apart from experimental uncertainties, lies therefore in the physical model used in the DSMC calculations. The largest uncertainty in the physical model is related to the gas-surface interaction model. It also has the biggest impact on the thrust slope compared to the molecular interaction potential, chamber conditions, or facility background gas pressure. A number of computations have therefore been performed for incomplete energy and momentum accommodation.

It is suggested by Arkilic, et al.[21] that a tangential momentum accommodation coefficient of 0.8 fits best for low Reynolds number flows. The results for the Maxwell model with 80 percent diffuse and 20 percent specular reflection are given in Fig. 12. Note that the energy accommodation coefficient is not very important since the wall temperature is equal to the stagnation temperature. An addition of surface specularity results in larger thrust for the nozzle flow in the entire range of Reynolds numbers. The general trend of the numerical points is even flatter than for the fully diffuse surface accommodation, especially for low Reynolds numbers where it strongly overpredicts the experimental values.

A close examination of the surface structure inside the actual nozzle manifested a very rough, groove-like structure, as illustrated in Fig. 3, with micron-size grooves set out perpendicular to the main flow direction. The evident surface roughness prompted the authors to introduce a simple model to simulate the roughness. In this model, a fraction of particles, α, is reflected diffusely on the surface, and a complementary fraction of particles, $(1-\alpha)$, is reflected with velocities both tangential and normal to the surface, v_τ and v_η respectively, taking an opposite sign as compared to the incident particle velocities. This type of reflection is hereafter referred to as antispecular. The diffuse-antispecular reflection kernel may be written as

$$K(\mathbf{v} \to \mathbf{v}') = (1-\alpha)\delta(\mathbf{v} - \mathbf{v}' + 2\mathbf{n}v_\eta + 2\tau v_\tau) + \alpha \frac{v_\eta}{2\pi}\left(\frac{m}{kT_W}\right)^2 \exp\left[-\frac{mv^2}{2kT_W}\right] \qquad (6)$$

The results of computations with $\alpha = 80$ (80 percent diffuse and 20 percent antispecular) are also shown in Fig. 12. It is clearly seen that whereas the points generally fall further from the experimental data than for the fully diffuse model, the diffuse-antispecular model predicts a thrust ratio slope close to the experimental one.

The comparison of the experimental and computed nozzle-to-orifice thrust ratios for molecular nitrogen is presented in Fig. 13. The general trend observed for the helium flow, where the numerical results were close to the measurements for the moderate Reynolds numbers, holds for the nitrogen flow as well.

C. Impact of the nozzle geometry

Previous numerical studies[6] of low Reynolds number nozzle flows analyzed the variation of the propulsive efficiency for different nozzle contours: conical, bell and trumpet. Zelesnik, et al[6] showed that the trumpet-shaped nozzle has about 5% higher efficiency compared to a conical nozzle for a stagnation temperature of approximately 300K. However, the easier to manufacture conical nozzle was shown to have a higher mass discharge coefficient.

In an attempt to define an optimum conical diverging nozzle configuration in the low Reynolds number regime, a set of computations has been performed for different geometrical configurations, with varied nozzle length and diverging section angle. The results were obtained for helium test gas and Reynolds numbers of 60 and 200. The surface accommodation in these computations was assumed to be fully diffuse.

To better understand the impact of the viscous effects on the nozzle efficiency for different nozzle geometries and chamber pressures, the specific impulse has been calculated as a function of the axial distance from the nozzle throat to the exit. Figure 14a shows the specific impulse profiles for three values of the nozzle length for $\mathrm{Re}^{*} = 60$. Consider first the baseline length of $\mathrm{L} = 1.07 \times 10^{-2} m$. Figure 14a shows that the specific impulse increases sharply over the first millimeter past the throat. Further downstream the specific impulse had a maximum and then decreased toward the nozzle exit plane as the influence of the viscous layer increases. Note that the maximum that occurs at $X \approx 0.4L$ was about 5% larger than that at the nozzle exit. The numerical results indicated that shortening the nozzle generally resulted in higher axial flow velocities at the nozzle exit plane close to the centerline due to a smaller impact of the viscous layer. However, the total I_{sp} increase amounts to only about 4% when the nozzle was three times shorter than the baseline case for $\mathrm{Re}^{*} = 60$.

As expected, an increase in the Reynolds number resulted in better nozzle efficiencies, as shown in Fig. 14b for $\mathrm{Re}^* = 200$ and three values of the nozzle length. Still, there was a maximum in the specific impulse observed inside the nozzle. The location of the maximum shifted downstream as compared to $\mathrm{Re}^* = 60$ due to the thinner viscous layer. The value of I_{sp} at the nozzle exit was about 2% lower than the maximum value inside the nozzle. The shortening of the nozzle causes about a 1% decrease with the relative position of the maximum being closer to the exit plane for shorter nozzles. A smaller influence of the viscous layer for larger Reynolds number flows was the reason for an insignificant impact of the nozzle length. The difference between the cases of L/2 and L/3 in terms of the nozzle efficiency was less than 1%.

The second nozzle geometry parameter varied was the angle of the diverging section. It is well known that conventional high Reynolds number conical nozzles are usually designed with a half-angle of about 15°, where the nozzle efficiency is maximum. For low Reynolds numbers, the viscous effects become a significant issue that degrades nozzle performance. Therefore, it appeared reasonable to increase the half-angle of the diverging section in order to improve the efficiency. The numerical studies in this work were carried out for the half-angle from 20° (baseline geometry) up to 40°. The angle was increased while maintaining a constant diverging section wall length, l_w.

Specific impulse as a function of axial station for four different half-angle values and $\mathrm{Re}^* = 60$ is given in Fig. 15a. While the general shape of the I_{sp} distribution does not change significantly with angle, there were several important effects associated with the angle increase. In contrast to the nozzle length change at a constant angle, where the flow was essentially constant over the first millimeter from the throat, the varying angle impacted the specific impulse immediately after the throat. A larger angle caused higher values of axial velocity, which

generally resulted in higher thrust and I_{sp} in the diverging section of the nozzle. Further downstream, the viscous layer decreased the nozzle efficiency, which was especially pronounced for smaller angles. A noticeably better nozzle performance was seen for larger angles. Every 5° increase in the angle resulted in about a 2% increase in the specific impulse at the nozzle exit plane for $\mathrm{Re}^{*} = 60$. At larger Reynolds numbers, the increase of the nozzle angle does not have a strong impact on the flow in the region of the throat, as illustrated in Fig. 15b.

The thrust and specific impulse results for all geometric conditions are summarized in Table 2. The general conclusion that can be drawn from Table 2 is that the increase of the nozzle angle and/or decrease of the nozzle length increased the thrust and improved the nozzle efficiency for Reynolds numbers less than approximately 100. This geometric improvement decreased with increasing Reynolds number, and is within one or two percent for all geometries considered at $\mathrm{Re}^{*} = 200$.

Numerical and Experimental Uncertainties

There are several uncertainties associated with the experimental effort in this study. First, corrections to the force measurements due to the facility background gas have not been incorporated into the data analysis. However, a previous study[15] indicated that the thrust may be effected by less than 0.5% at the experimental conditions of this work. Second, the standared deviation of the stagnation pressure and mass flow measurements was found to be within approximately 1% over the range used. Third, thrust stand calibration of deflection versus applied force has been approximated to be within 3%. For a given applied force to the thrust stand, the standard deviation of the stand's deflection was less than 1%; however, the accuracy of the calibration system must also be taken into account. Finally, there was some error

associated with the manufacturing of the orifice and nozzle. In general, the nozzle throat diameter is known to within 0.5%. Because the orifice was machined from a thin tantalum shim, the measurement of its diameter is not quite as accurate and is estimated to be within approximately 2%.

In addition to the experimental uncertainties, there are a number of numerical uncertainties. Grid resolution, the maximum number of simulated molecules, effects of the subsonic boundary conditions, and the gas-gas collision models all account for a numerical uncertainty estimated to be on the order of 1 to 2%. The effects of the nozzle surface roughness present in the experimental device are not known, although a simple diffuse-anti-specular model was used. However, it is not known to what extent the nozzle surface roughness contributes to uncertainties in either the numerical or experimental data.

Conclusions

Low Reynolds number flows through nozzle and orifice geometries have been investigated both numerically and experimentally. The DSMC results show that the viscous effects dominate the flow for $Re^* = 60$. This result has been seen in previous studies[1] and prompted the investigation of thin-walled orifices for thrust generation, since presumably an orifice would not exhibit large viscous interaction regions. Experimental results indicate that at $Re^* < 100$ the thrust generated by an orifice is indeed larger than that of the nominal conical nozzle for helium and nitrogen. However, the nozzle remains more efficient (based on I_{sp}) than the orifice throughout the range of I_{sp} investigated. There is a minimum in the nozzle to orifice specific impulse ratio around $Re^* = 60$ for helium. Therefore at some Reynolds numbers, it may

be advantageous to use a simple orifice geometry in this range over a nozzle geometry that is complicated to fabricate.

In general, the experimental and numerical results for the nozzle to orifice thrust ratio are in good agreement (within a few percent). The results obtained with an anti-specular gas-surface interacton model for DSMC show better qualitative agreement with the slope of the thrust ratio data than the standard Maxwell model. The anti-specular model was investigated based on scanning electron microscope images of the nozzle's surface roughness caused by the machining process. Although the exact influence of the surface roughness is unknown, it appears to have a measurable effect on the nozzle's performance.

Once the DSMC model results were verified using experimental data, the model was used to assess geometrical variations on the conical nozzle's performance. Both the diverging section length and angle were varied to assess the effect on nozzle performance. Little effect was seen in improving the performance for $Re^* = 200$ where all variations were within 2%. However, an 8% improvement in I_{sp} was seen for a $Re^* = 60$ helium flow when the expansion angle was doubled from 20° to 40°. At $Re^* = 60$, it was also shown that shortening the diverging section length improved the nozzle's performance. Previous studies[6] have shown that using trumpet geometries may further improve the performance over a conical geometry by as much as 5% at low Reynolds number. Therefore, reasonable improvement of nozzle performance for $Re^* < 100$ can be realized through the use of numerical simulations to optimize geometry.

Acknowledgments

This work was supported in part by the U.S. Air Force Office of Scientific Research and the Propulsion Directorate of the Air Force Research Laboratory at Edwards Air Force Base, California. The authors wish to thank Mr. Andrew Jamison and Mr. Taylor Lilly for their invaluable assistance with this research.

References

[1]Ivanov, M., Markelov, G., Ketsdever, A., and Wadsworth, D., "Numerical Study of Cold Gas Micronozzle Flows," *AIAA Paper 99-0166*, January 1996.

[2]Ketsdever, A., "Thrust Measurements of an Underexpanded Orifice in the Transitional Regime," *Proceedings of the 23rd International Symposium on Rarefied Gas Dynamics*, edited by A. Ketsdever and E.P. Muntz, American Institute of Physics, New York, 2002, pp. 1057-1064.

[3]Alexeenko, A., Gimelshein, S., Levin, D., Ketsdever, A., and Ivanov, M., "Measurements and Simulation of Orifice Flow for Micropropulsion Testing," *Journal of Propulsion and Power*, Vol. 19, No. 4, 2003, pp. 588-594.

[4]Kim, S., "Calculations of Low-Reynolds-Number Resistojet Nozzles," *Journal of Spacecraft and Rockets*, Vol. 31, No. 2, 1994, pp. 259-264.

[5]Boyd, I., Jafry, Y., and Vanden Beukel, J., "Particle Simulations of Helium Microthruster Flows," *Journal of Spacecraft and Rockets*, Vol. 31, No. 2, 1994, pp. 271-277.

[6]Zelesnik, D., Micci, M., and Long, L., "Direct Simulation Monte Carlo Model of Low Reynolds Number Nozzle Flows," *Journal of Propulsion and Power*, Vol. 10, No. 4, 1994, pp. 546-553.

[7]Chung, C.-H., Kim, S., Stubbs, R., and De Witt, K., "Low-Density Nozzle Flow by the Direct Simulation Monte Carlo and Continuum Mehtods," *Journal of Propulsion and Power*, Vol. 11, No. 1, 1995, pp. 64-78.

[8]Alexeenko, A., Levin, D., Gimelshein, S., Collins, R., and Reed, B., "Numerical Study of Flow Structure and Thrust Performance for 3-D MEMS-Based Nozzles," *AIAA Paper 2002-3194*, June 2002.

[9]Murch, C., Broadwell, J., Silver, A., and Marcisz, T., "Low-Thrust Nozzle Performance," *AIAA Paper 68-091*, January 1968.

[10]Rothe, D., "Electron-Beam Studies of Viscous Flow in Supersonic Nozzles," *AIAA Journal*, Vol. 9, No. 5, 1971, pp. 804-810.

[11]Whalen, M., "Low Reynolds Number Nozzle Flow Study," *NASA Technical Memorandum 100130*, July 1987.

[12]Lempert, W., Boehm, M., Jiang, N., Gimelshein, S., and Levin, D., "Comparison of Molecular Tagging Velocimetry Data and Direct Simulation Monte Carlo Simulation in Supersonic Micro Jet Flows," *Expt. In Fluids,* Vol. 34, 2003, pp. 403-411.

[13]Jamision, A., and Ketsdever, A., "Low Reynolds Number Performance Comparison of an Underexpanded Orifice and a DeLaval Nozzle," *Proceedings of the 23rd International Symposium on Rarefied Gas Dynamics*, edited by A. Ketsdever and E.P. Muntz, American Institute of Physics, New York, 2002, pp. 557-564.

[14]Jamison, A., Ketsdever, A., Muntz, E.P., "Gas Dynamic Calibration of a Nano-Newton Thrust Stand," *Review of Scientific Instruments*, Vol. 73, No. 10, 2002, pp. 3629-3637.

[15]Ketsdever, A., "Facility Effects on Performance Measurements of Micropropulsion Systems Which Utilize Gas Expansion," *Journal of Propulsion and Power*, Vol. 18, No. 4, 2002, pp. 797-804.

[16]Selden, N., Ketsdever, A., "Comparison of Force Balance Calibration Techniques for the nano-Newton Range," Review of Scientific Instruments, Vol. 74, No. 12, 2003, pp. 5249-5254.

[17]Ivanov, M.S., Markelov, G.N., Gimelshein, S.F. "Statistical simulation of reactive rarefied flows: numerical approach and applications," *AIAA Paper 98-2669*, June 1998.

[18]Ivanov, M.S., Rogasinsky, S.V. "Analysis of the numerical techniques of the direct simulation Monte Carlo method in the rarefied gas dynamics," *Soviet J. Numer. Anal. Math. Modeling*, Vol. 3, No. 6, 1988, pp. 453-465.

[19]Borgnakke, C. and Larsen, P. S., "Statistical collision model for Monte Carlo simulation of polyatomic gas mixture," *J. Comp. Phys.* 18:405-420, 1975.

[20]Gimelshein, S.F., Boyd, I.D., Ivanov, M.S. "Modeling of internal energy transfer in plume flows of polyatomic molecules by the DSMC method," *AIAA Paper 99-0738*. Reno, NV, January 1999.

[21]Arkilic, E. B., Breuer, K. S., and Schmidt, M. A., "Mass flow and tangential momentum accommodation in silicon micromachined channels," *Journal of Fluid Mechanics*, Vol. 437, 2001, pp. 29-43.

Table and Figure Captions:

Table 1: Numerical data for the performance of the nominal orifice and nozzle geometries as a function of Reynolds number.

Table 2: Numerical data for the performance of various nozzle geometries.

Figure 1: Thin-walled orifice geometry.

Figure 2: Experimental geometry of the conical DeLaval nozzle.

Figure 3: SEM imaging showing the surface roughness of the expanding section of the conical nozzle.

Figure 4: Predicted Mach number contours for helium orifice flow at $Re^{*} = 10$ (top) and 200 (bottom).

Figure 5: Predicted Mach number contours for helium flow inside the nozzle at $Re^{*} = 10$ (top) and 200 (bottom).

Figure 6: Predicted T_x/T contours for helium orifice flow at $Re^{*} = 10$ (top) and 200 (bottom).

Figure 7: Predicted T_x/T contours for helium flow inside the nozzle at $Re^{*} = 10$ (top) and 200 (bottom).

Figure 8: Predicted axial velocity profiles along the orifice plane for different Reynolds numbers for a helium flow. Y=0 corresponds to the symmetry axis.

Figure 9: Predicted axial velocity profiles across the nozzle exit plane for different Reynolds numbers for a helium flow. Y=0 corresponds to the symmetry axis.

Figure 10: Orifice thrust comparison between experimental and numerical data for helium.

Figure 11: Nozzle thrust comparison between experimental and numerical data for helium.

Figure 12: Ratio of the nozzle to orifice thrust for helium as a function of Reynolds number.

Figure 13: Ratio of the nozzle to orifice thrust for nitrogen as a function of Reynolds number.

Figure 14: Impact of the nozzle length on performance for helium. a) $Re^* = 60$, b) $Re^* = 200$.

Figure 15: Impact of the nozzle expansion angle on performance for helium. a) $Re^* = 60$, b) $Re^* = 200$.

Re*	Kn	P_0 [Pa]	T_o [N]	T_n [N]	T_n/T_o	Isp_o [s]	Isp_n [s]	Isp_n / Isp_o
0.02	48.58	3.59E-01	1.41E-07	1.28E-07	0.907	102.48	127.09	1.24
0.2	4.883	3.57E+00	1.43E-06	1.26E-06	0.881	102.91	126.17	1.23
2	0.488	3.57E+01	1.64E-05	1.38E-05	0.805	108.23	127.57	1.18
5	0.195	8.92E+01	4.81E-05	3.83E-05	0.796	114.19	128.67	1.13
10	0.098	1.78E+02	1.13E-04	8.89E-05	0.786	122.78	129.85	1.06
23	0.042	4.10E+02	3.02E-04	2.49E-04	0.825	128.96	132.79	1.03
60	0.016	1.07E+03	8.69E-04	8.01E-04	0.922	138.42	140.53	1.02
90	0.011	1.61E+03	1.34E-03	1.30E-03	0.970	141.34	145.01	1.03
120	0.008	2.14E+03	1.79E-03	1.81E-03	1.01	143.61	148.86	1.04
200	0.005	3.57E+03	3.04E-03	3.28E-03	1.08	144.62	155.38	1.07

Table 1

Angle (deg)	Re*	Length	T_n (N)	Isp_n (s)	Isp_n / Isp_{Nom}
20	60	Nominal l_w	8.01E-04	140.53	1.00
		$l_w/2$	8.25E-04	144.14	1.03
		$l_w/3$	8.33E-04	145.55	1.04
	200	Nominal l_w	3.28E-03	155.38	1.00
		$l_w/2$	3.29E-03	157.14	1.01
		$l_w/3$	3.29E-03	157.23	1.01
25	60	l_w	8.33E-04	144.14	1.03
		$l_w/2$	8.42E-04	146.43	1.04
	200	l_w	3.32E-03	157.57	1.01
		$l_w/2$	3.34E-03	158.17	1.02
30	60	l_w	8.58E-04	148.14	1.05
	200	l_w	3.33E-03	159.12	1.02
40	60	l_w	8.82E-04	151.76	1.08
	200	l_w	3.34E-03	159.10	1.02

Table 2

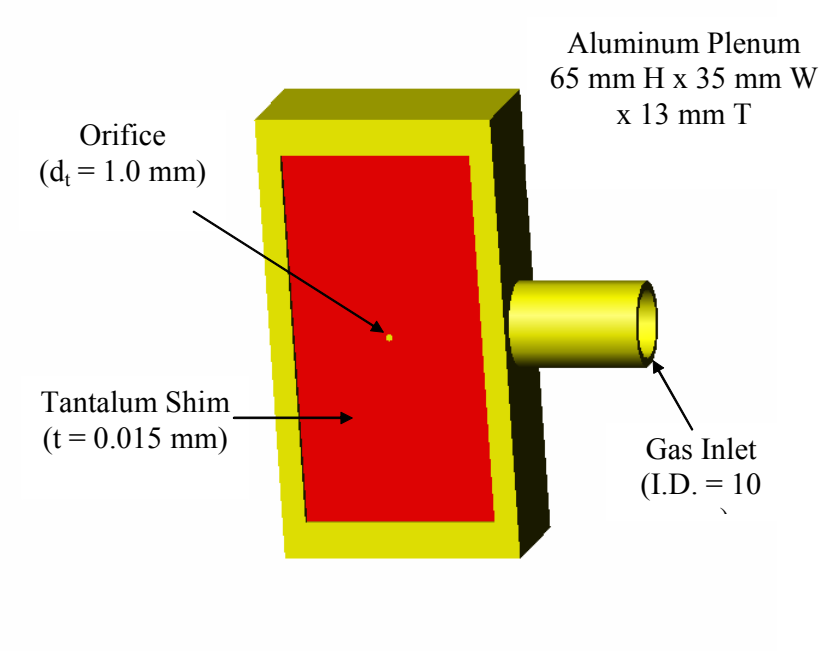
Aluminum Plenum
65 mm H x 35 mm W
x 13 mm T
Orifice
(d_t = 1.0 mm)
Tantalum Shim
(t = 0.015 mm)
Gas Inlet
(I.D. = 10

Figure 1

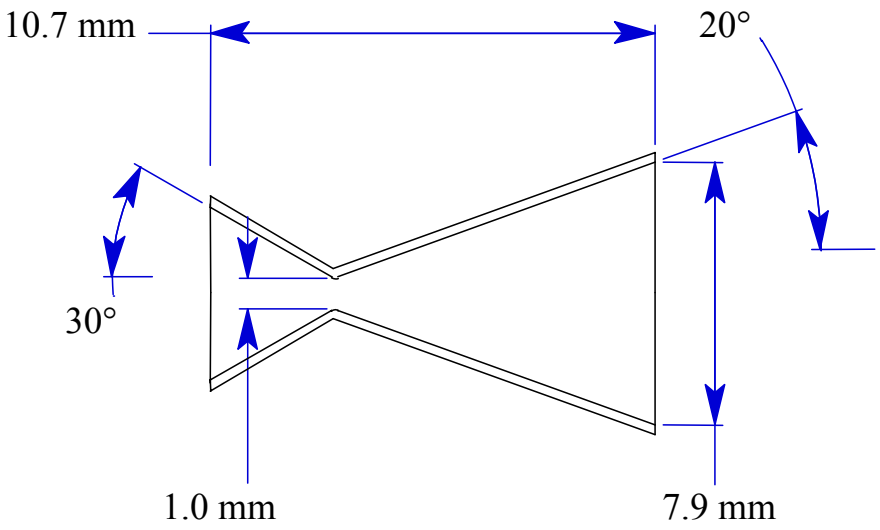

Figure 2

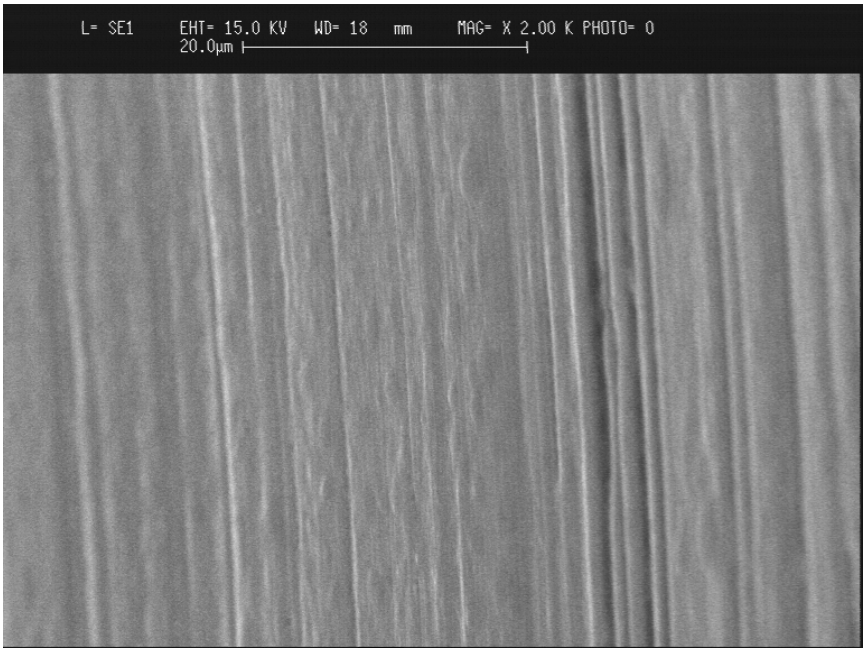

Figure 3

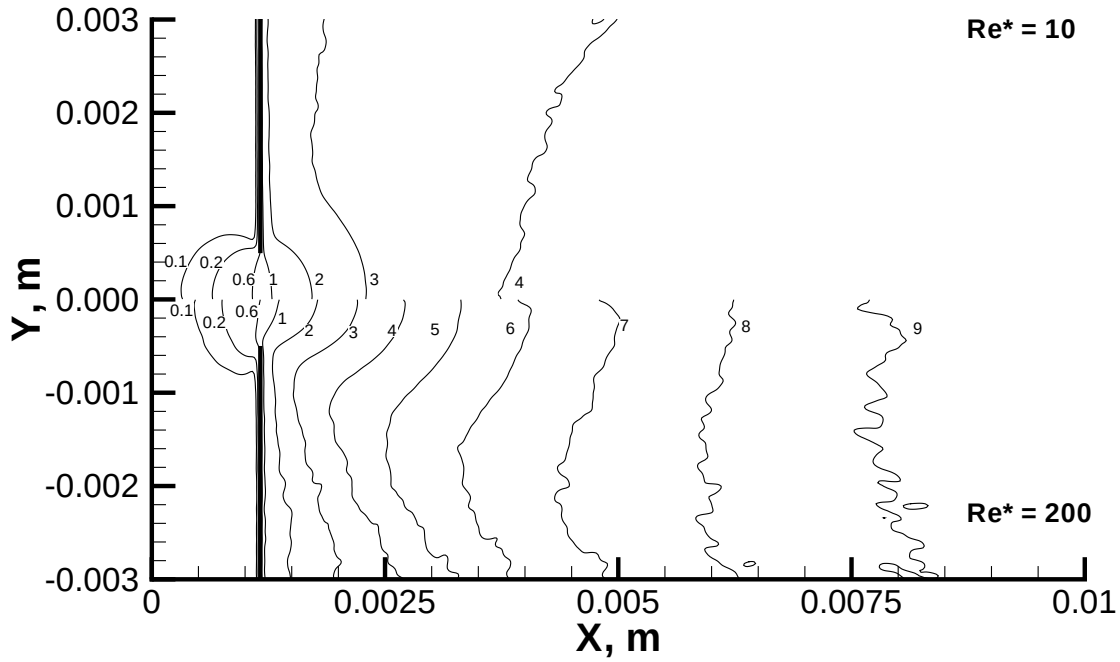
Re* = 10
Re* = 200
Y, m
X, m
0.003
0.002
0.001
0.000
-0.001
-0.002
-0.003
0
0.0025
0.005
0.0075
0.01
0.1
0.2
0.6
1
2
3
4
5
6
7
8
9

Figure 4

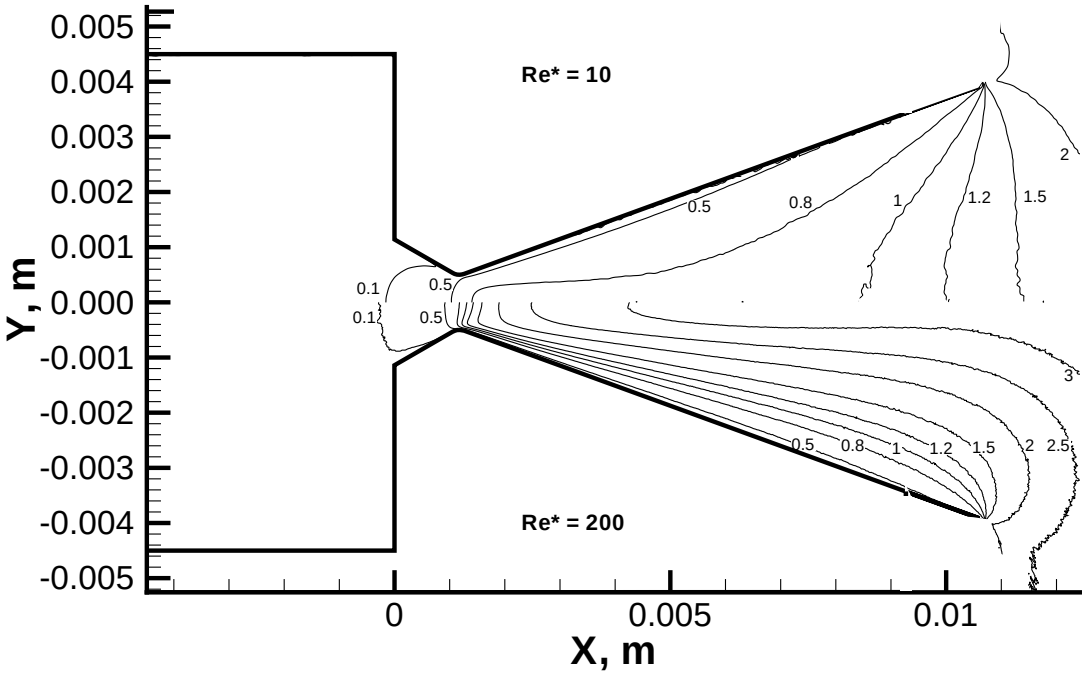
Re* = 10
Re* = 200
0.1
0.5
0.8
1
1.2
1.5
2
2.5
3
Y, m
X, m
0.005
0.004
0.003
0.002
0.001
0.000
-0.001
-0.002
-0.003
-0.004
-0.005
0
0.005
0.01

Figure 5

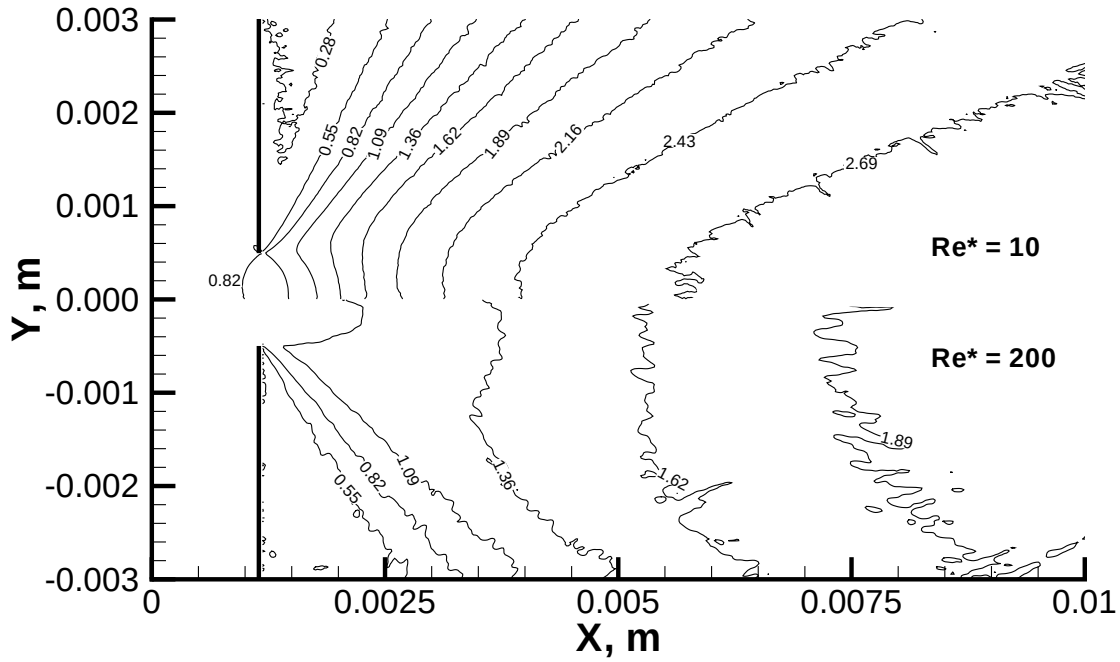
0.003
0.002
0.001
0.000
-0.001
-0.002
-0.003
Y, m
0
0.0025
0.005
0.0075
0.01
X, m
0.28
0.55
0.82
1.09
1.36
1.62
1.89
2.16
2.43
2.69
Re* = 10
Re* = 200

Figure 6

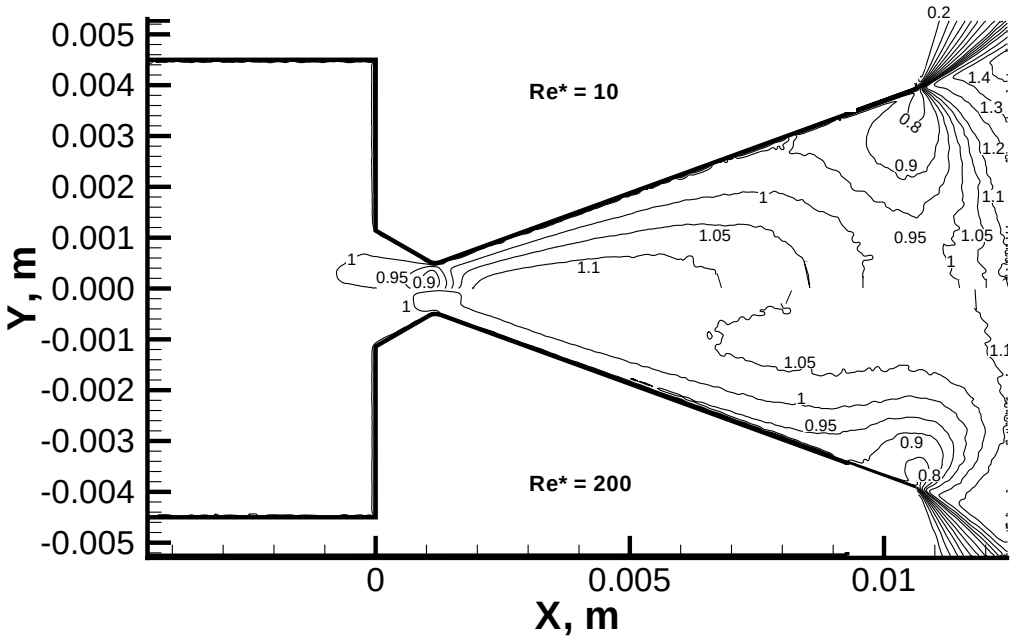
Re* = 10
Re* = 200
Y, m
X, m
0.005
0.004
0.003
0.002
0.001
0.000
-0.001
-0.002
-0.003
-0.004
-0.005
0
0.005
0.01
0.2
0.8
0.9
1
1.1
1.2
1.3
1.4
1.05
0.95

Figure 7

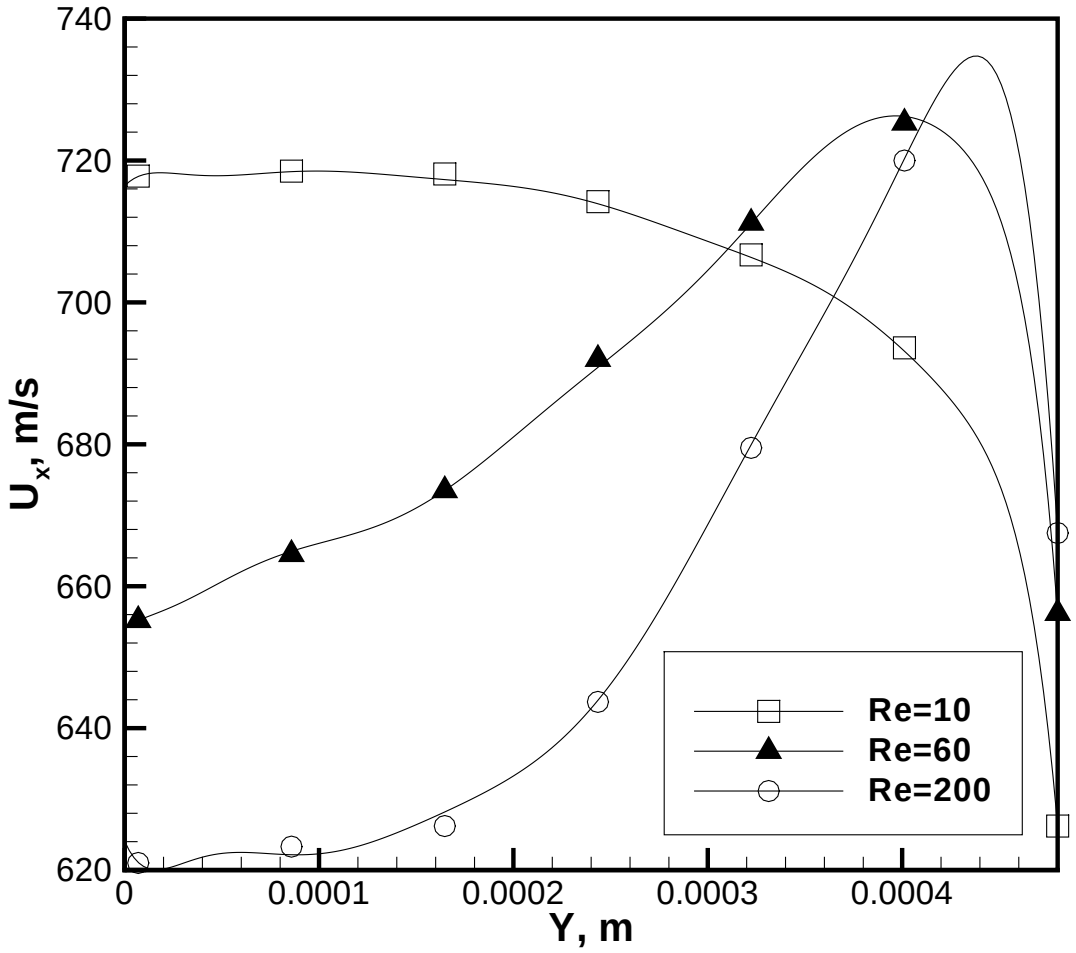
740
720
700
680
660
640
620
U_x, m/s
0
0.0001
0.0002
0.0003
0.0004
Y, m
Re=10
Re=60
Re=200

Figure 8

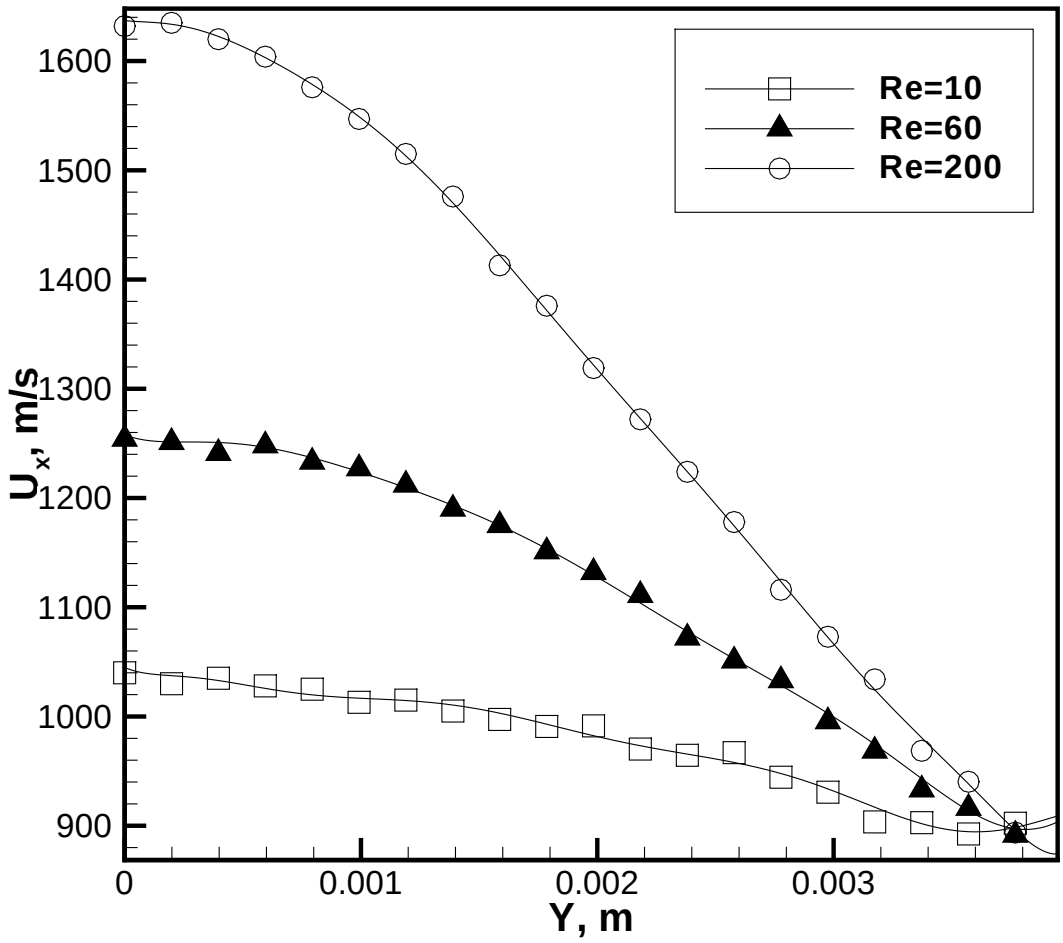
Re=10
Re=60
Re=200
1600
1500
1400
1300
1200
1100
1000
900
U_x, m/s
0
0.001
0.002
0.003
Y, m

Figure 9

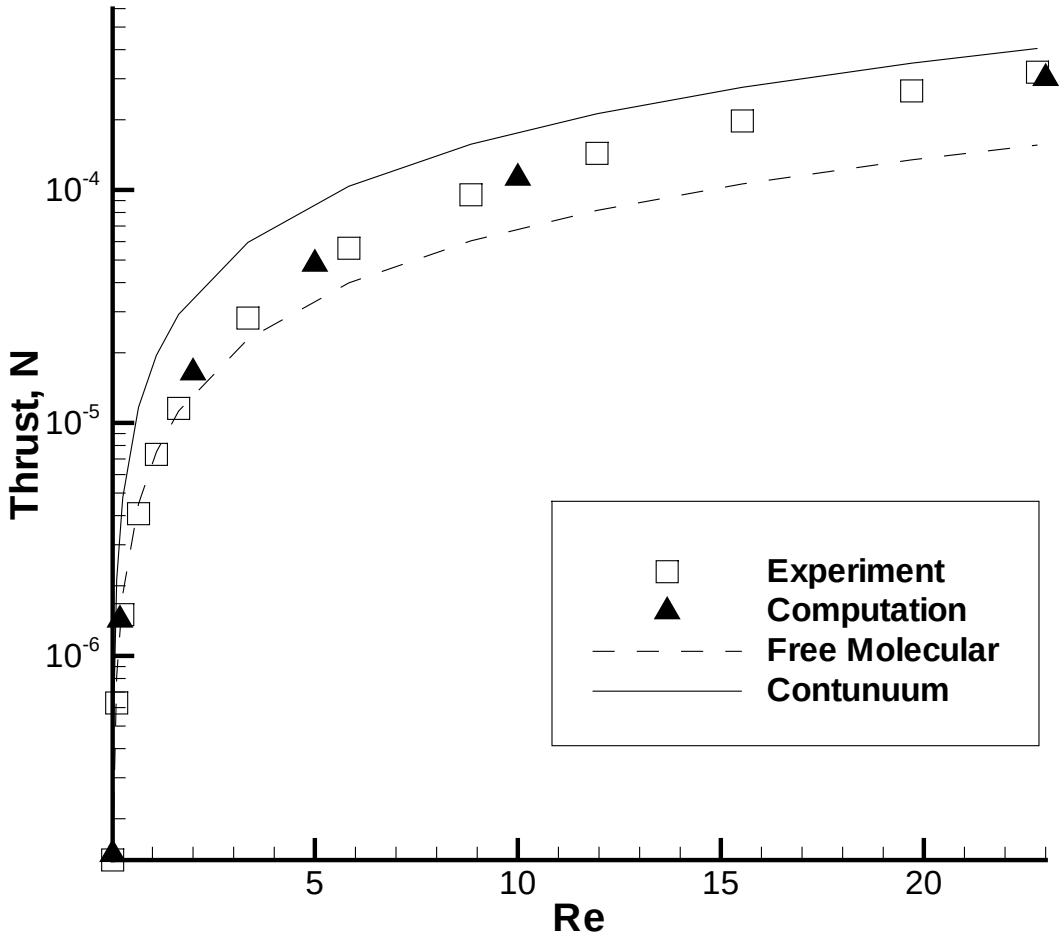
Thrust, N
10-4
10-5
10-6
5
10
15
20
Re
Experiment
Computation
Free Molecular
Contunuum

Figure 10

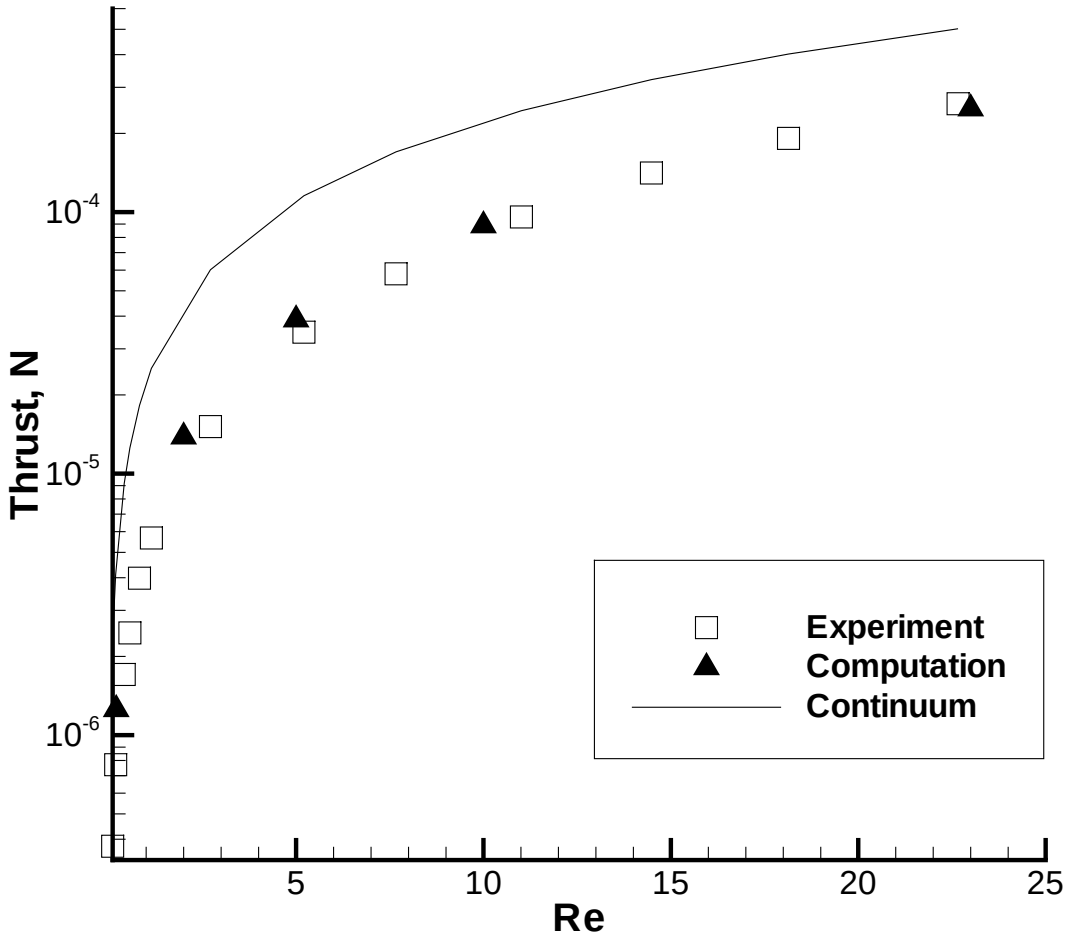
Thrust, N
10-4
10-5
10-6
5
10
15
20
25
Re
Experiment
Computation
Continuum

Figure 11

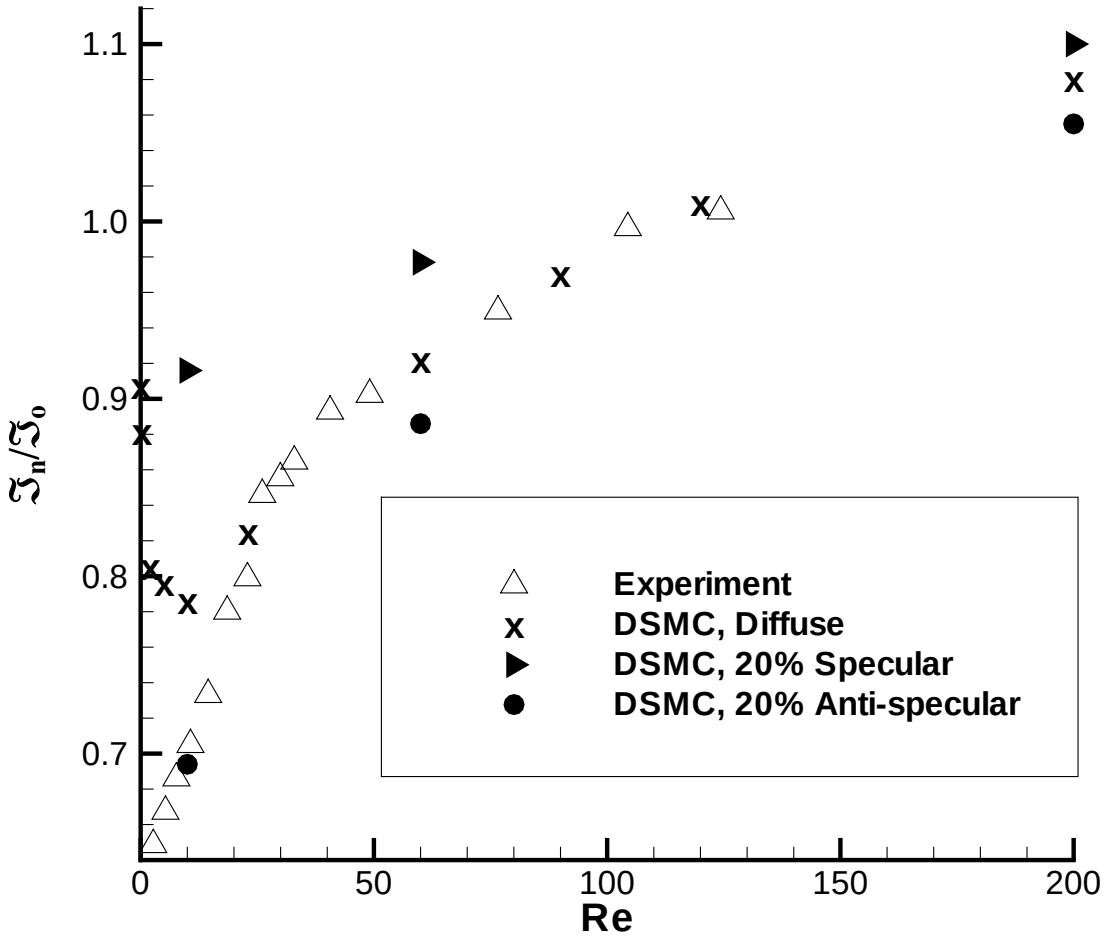
1.1
1.0
0.9
0.8
0.7
$\Im_n/\Im_o$
0
50
100
150
200
Re
Experiment
DSMC, Diffuse
DSMC, 20% Specular
DSMC, 20% Anti-specular

Figure 12

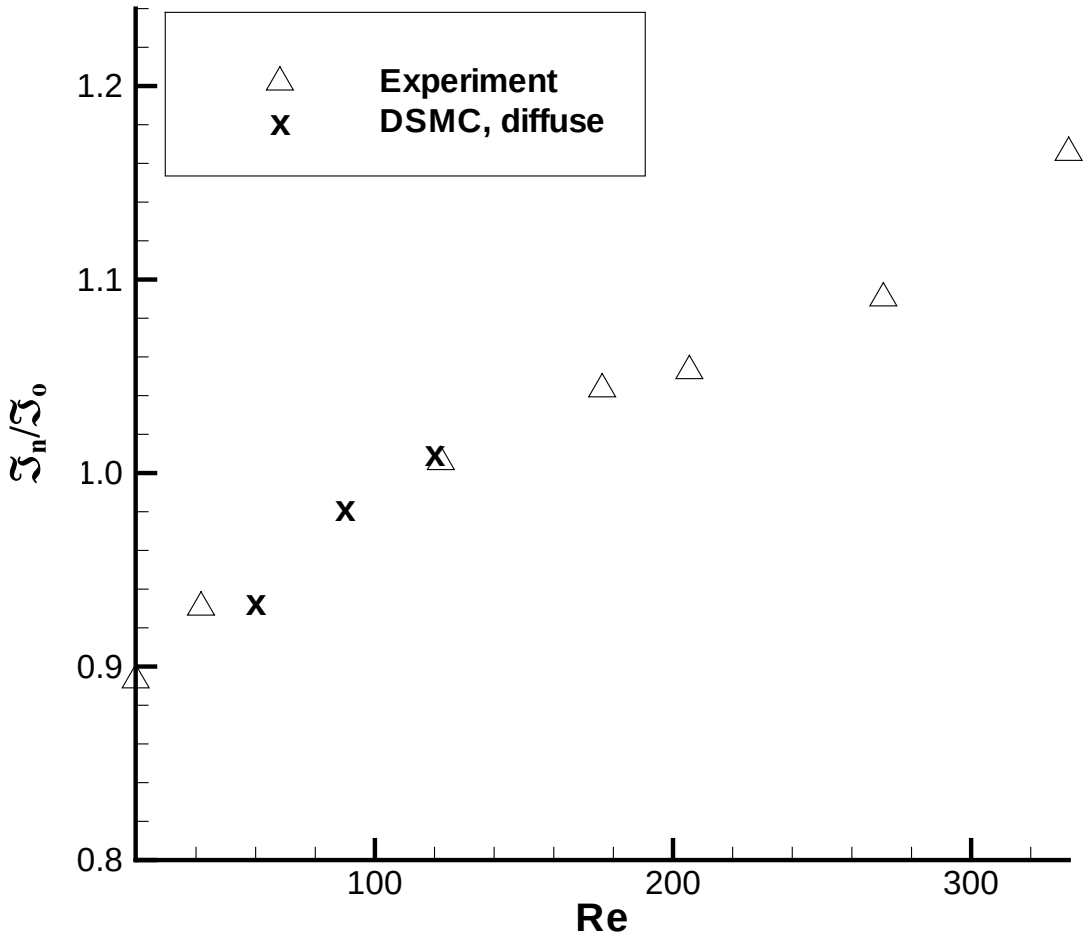

Figure 13

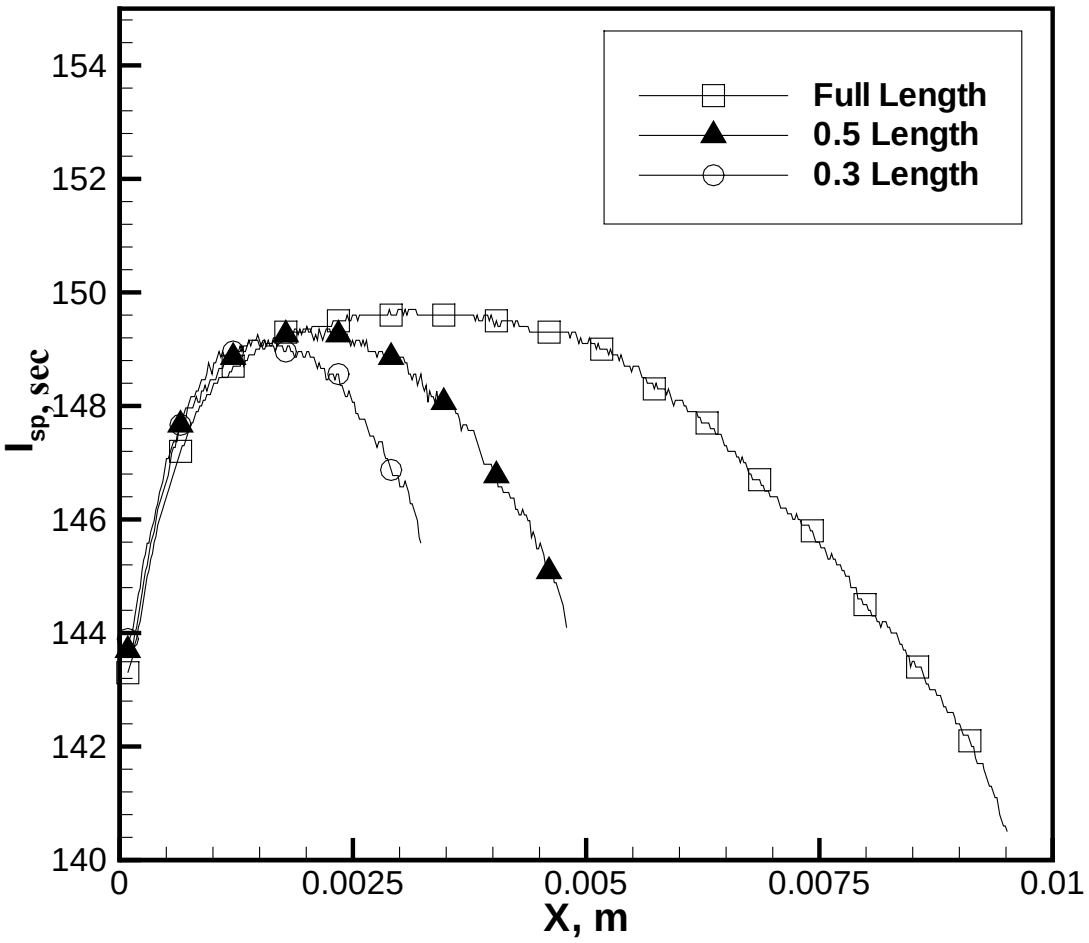
Full Length
0.5 Length
0.3 Length
154
152
150
148
146
144
142
140
0
0.0025
0.005
0.0075
0.01
X, m
I_{sp}, sec

Figure 14(a)

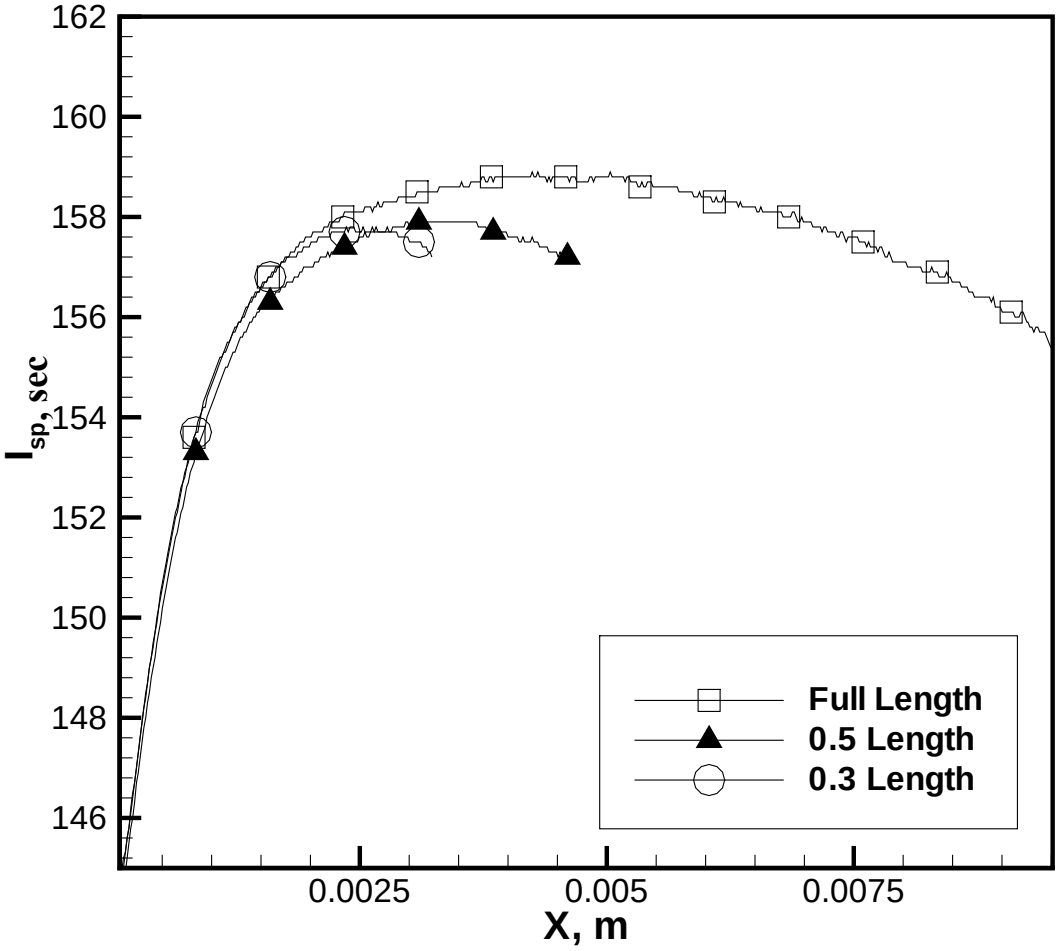
162
160
158
156
154
152
150
148
146
I_{sp}, sec
0.0025
0.005
0.0075
X, m
Full Length
0.5 Length
0.3 Length

Figure 14(b)

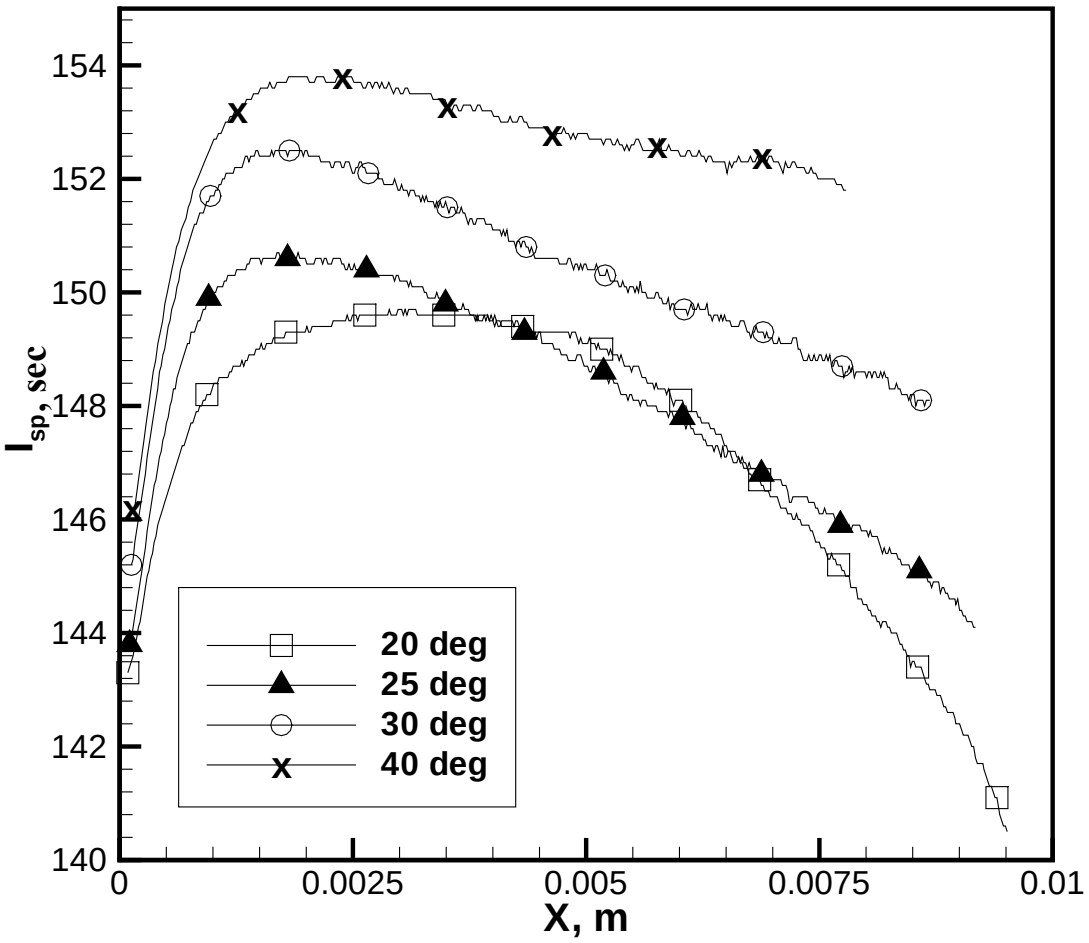
154
152
150
148
146
144
142
140
0
0.0025
0.005
0.0075
0.01
X, m
I_{sp}, sec
20 deg
25 deg
30 deg
40 deg

Figure 15(a)

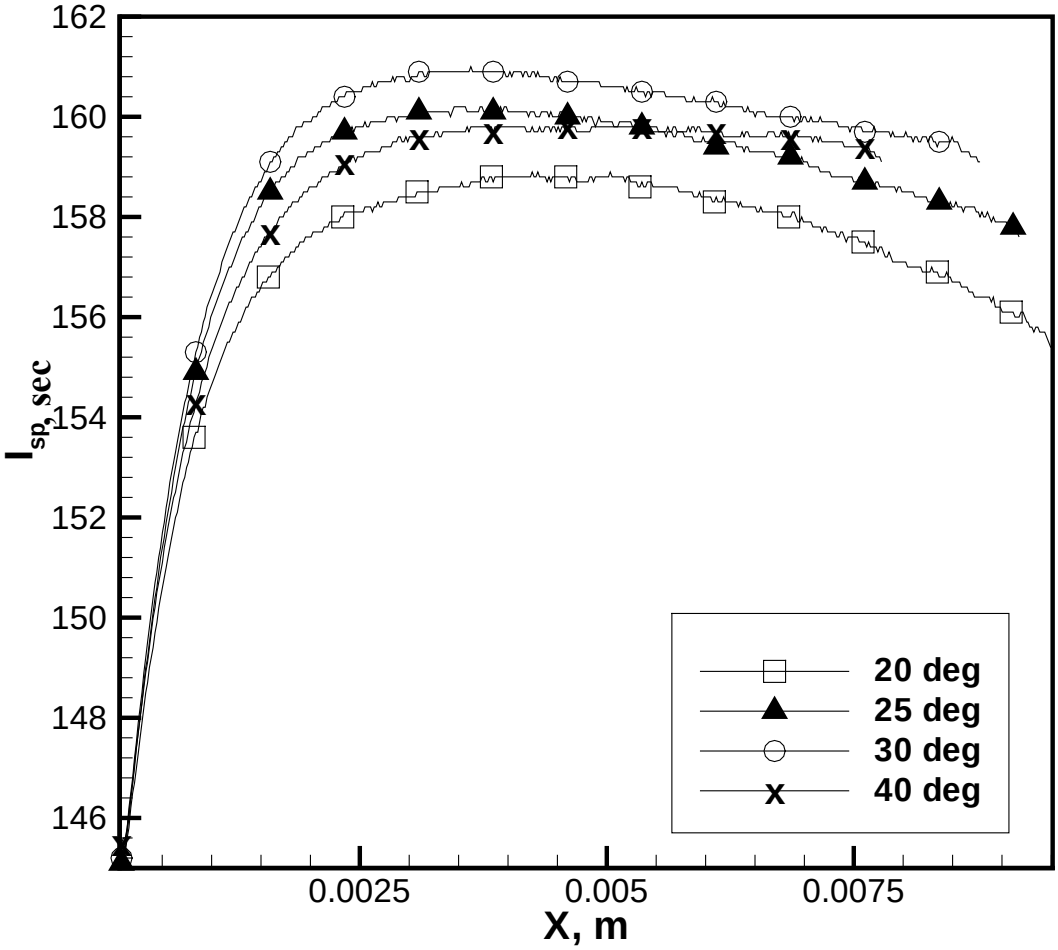
162
160
158
156
154
152
150
148
146
I_{sp}, sec
0.0025
0.005
0.0075
X, m
20 deg
25 deg
30 deg
40 deg

Figure 15(b)